Cryo-EM structure of the bacterial effector protein SipA bound to F-actin reveals a unique mechanism for filament stabilization

Emily Guo[1], Steven Z. Chou[2], Maria Lara-Tejero[1], and Jorge E. Galán[1]*

[1]Department of Microbial Pathogenesis, Yale University School of Medicine, New Haven, CT 06536, and [2]Department of Molecular Biology and Biophysics, UConn Health, Farmington, CT 06030

Key words: bacterial pathogenesis, *Salmonella* pathogenesis, actin dynamics, type III protein secretion, host-pathogen interactions

* For correspondence: jorge.galan@yale.edu

ABSTRACT

The bacterial pathogen *Salmonella* spp. modulates cellular processes by delivering effector proteins through its type III secretion systems. Among these effectors, SipA facilitates bacterial invasion and promotes intestinal inflammation. The mechanisms by which this effector carries out these functions are incompletely understood although SipA's ability to modulate actin dynamics is central to some of these activities. Here we report the cryo-EM structure of SipA bound to filamentous actin. We show that this effector stabilizes actin filaments through unique interactions of its carboxy terminal domain with four actin subunits. Furthermore, our structure-function studies revealed that SipA's actin-binding activity is independent from its ability to stimulate intestinal inflammation. Overall, these studies illuminate critical aspects of *Salmonella* pathogenesis, and provide unique insight into the mechanisms by which a bacterial effector modulates actin dynamics.

MAIN

Salmonella enterica serovars can cause a range of human illnesses, from self-limiting gastroenteritis (i.e. food poisoning) to systemic, life-threatening infections (i.e. typhoid fever), resulting in an estimated 200,000 annual death worldwide (1-8). Central to their pathogenesis is their ability to invade intestinal epithelial cells and cause intestinal inflammation (4, 5, 7, 8). Epithelial cell invasion is orchestrated by the combined activity of several effectors of a type III protein secretion system (T3SS) encoded within its pathogenicity island 1 (SPI-1) (9-12). These effectors trigger cellular responses that result in the reorganization of the actin cytoskeleton leading to the formation of large lamellipodia-like structures or membrane ruffles that internalize the bacteria into a membrane-bound compartment, the *Salmonella*-containing vacuole.

Three of these effector proteins, SopE, SopE2, and SopB, play a central role in the internalization process by stimulating Rho-family GTPases, which initiate downstream signaling leading to the WASH/WAVE-dependent activation of endogenous actin nucleators, such as the Arp2/3 complex (13-18). SopE and its close homolog SopE2 directly target the Rho-family GTPases Rac1 and Cdc42 acting as potent exchange factors (13, 19). In contrast, SopB activates endogenous cellular exchange factors by fluxing phosphoinositides through its phosphoinositide-phosphatase activity (15).

Two other effectors, SipC and SipA, contribute to bacterial invasion by directly targeting actin (20, 21). Besides its role in T3SS-mediated protein translocation (22), SipC can nucleate and bundle actin filaments (21). A SipC mutant defective in actin-binding but proficient in T3SS-mediated protein translocation, showed a relatively small but significant defect in bacterial internalization (23), indicating an accessory but important role in bacterial cell entry. SipA plays a complex role in *Salmonella* pathogenesis. Through its carboxy-terminal actin-binding domain, SipA contributes to bacterial entry by reducing the critical concentration of actin required for its polymerization (20, 24). Furthermore, SipA stabilizes actin filaments and prevents the

depolymerizing action of F-actin-severing proteins such as ADF/Cofilin and gelsolin (25). Consequently, the absence of SipA results in a reduced size of the bacterial stimulated actin ruffles and decreased epithelial cell invasion (20, 25). In addition, through its amino-terminal domain, SipA modulates the intestinal inflammatory response to *Salmonella* by mechanisms that are not yet fully understood (26, 27). However, it remains unclear whether the actin-binding activity of SipA is related to this additional function since despite previous efforts (28), the lack of high resolution structural information on the SipA-actin interface has hampered the construction of SipA mutants that are essential to sort out this issue.

Similarly, due to the lack of structural information, the mechanisms by which SipA modulates actin dynamics are poorly understood. Although the crystal structure of the actin-binding domain of SipA in isolation is available (29), its atomic structure bound to F-actin is not. Previous low-resolution negative stained cryo-EM structures led to the proposal that SipA "staples" actin filaments through the deployment of two non-globular arms that reach out to opposing actin strands, presumably engaging actin in a similar manner to nebulin (29, 30). However, the lack of high-resolution structures has prevented the rigorous testing of such a model. Furthermore, machine learning–based approaches such as that afforded by Alpha Fold (31, 32), are inadequate to predict the structure of SipA bound to F-actin. In this study we report the cryo-EM structure of SipA bound to F-actin at 3.6 Å resolution. Our structure, validated by functional studies, clarifies the function of SipA, reveals a unique mechanism of F-actin stabilization by an actin-binding protein, and provides unique insight into the mechanisms of *Salmonella* invasion.

Results

Overall Structure of SipA decorated F-actin

The *S.* Typhimurium effector protein SipA is 685 amino acids in length and is composed of at least three domains: an N-terminal chaperone-binding domain, a central ~200 amino acid domain modeled by Alphafold as long unstructured loops, and a C-terminal actin-binding globular domain (Supplementary Fig. 1). We first attempted to purified full-length SipA using different tags and purification conditions. However, consistent with previous reports (29), all constructs containing the central region were insoluble. Therefore, to study the actin-stabilizing function of SipA we concentrated our efforts on its C-terminal domain (amino acids 447 to 685), which previous studies have found to contain all its actin-modulating activities (20, 29). Consistent with previous reports (20, 29), we found that purified $SipA_{447\text{-}685}$ interact with skeletal muscle actin with high affinity (0.54 μM) as determined by a co-sedimentation assay (Supplementary Fig. 2). Also, consistent with previous observations (20), negative stained actin filaments polymerized in the presence of SipA observed under the electron microscope showed a thicker and straighter appearance than filaments polymerized in its absence (Supplementary Fig. 3).

To determine the structure of the SipA-actin complex, purified G-actin was first polymerized to form filaments, then mixed with purified $SipA_{447\text{-}685,}$ and examined by single particle cryo-EM. We collected 4,740 movies, of which 2,370 were used for manual filament picking (see Methods). In total, 320,109 filament segments were boxed out for further analyses. The helical parameters of $SipA_{447\text{-}685}$-decorated actin filaments were determined by helical indexing of the averaged power spectrum. By applying helical symmetry in the EM reconstruction, we obtained a map with extra densities alongside both strands of the actin filaments, which were not present in actin filaments alone and therefore assumed to correspond to SipA (Fig. 1). Notably, lower electron map occupancy of these extra densities was observed both in 2D class averages and in initial 3D reconstructions indicating a sub-stoichiometric presence of SipA on the actin filaments (Supplementary Fig. 4). DeepEMhancer (33) was applied to improve the map visibility and connectivity. A final map was produced with a global resolution of 3.6 Å determined by the Fourier shell correlation (FSC) at 0.143 cutoff (Supplementary Fig. 5). This map showed densities

corresponding to the side chains of most actin residues, as well as the bound nucleotide and the associated Mg^{2+} in polymerized actin, which allowed the unambiguous subsequent model building of SipA (see below).

The density corresponding to $SipA_{447-685}$ is compact and globular, with dimensions (30 Å x 40 Å x 40 Å) that correspond well with its previously solved crystal structure (PDB ID: 1Q5Z) (29) (Fig. 1). We also detected the presence of a poorly resolved non-globular extension at the C-terminus that inserts deep into F-actin. However, contrary to what has been previously reported (29), we did not observe any non-globular protrusions or arms that reach out to the opposite actin strands even though the same SipA construct was used in both studies. SipA decorates both sides of the actin filaments, following their helical symmetry (Fig. 1) and making contact mainly at the pockets between the two strands of the actin filament (see below).

Atomic model of SipA bound to F-actin

The atomic model of the SipA-F-actin complex was built by docking onto the EM map the crystal structure of SipA (PDB ID: 1Q5Z) (29) and ADP-Pi-actin (PDB ID: 6DJN) (34) into the reconstructed EM map using Chimera (35) and several rounds of model building and refinement with COOT (36) and Phenix (37). Residues 514-675 of SipA could be resolved in our map consisting of a globular domain that encompasses residues 514-657, and a C-terminal extension that comprises residues 658-675 (Fig. 2A). This is in accordance with previous observations indicating that the central domain of SipA, located immediately adjacent to the amino terminal end of its actin-binding domain, is unstructured, which was confirmed by AlphaFold modeling (31) (Supplementary Fig. 1). Alignment of the globular domain of SipA bound to actin with its crystal structure in solution revealed that actin-binding does not induce substantial conformational changes [a Cα root mean square deviation (RMSD) over residues 514-658: 0.843 Å] (Fig. 2B). Only minor local conformational changes in SipA were observed at its actin-binding surface. Similarly, only minor local conformational changes were noticeable in the actin filaments bound

to SipA mainly involving the D-loop region, with no detectable changes in the bound nucleotide, and the associated Mg^{2+} (Fig. 2C).

The SipA-associated density in our structure could be fully accounted in the modeled structure since in our cryo-EM map, SipA is seen interacting with actin as a globular structure (Fig. 2A). In addition, we observed a poorly resolved carboxy terminal extension of SipA, which inserts deep into the F-actin filament. We established that, as previously shown (29), this extension is required for the ability of SipA to polymerize G-actin although it appears dispensable for its ability to stabilize F-actin (Supplementary Fig. 6A-D). Furthermore, consistent with the functional importance of this extension, its deletion also affected the ability of *S*. Typhimurium to invade cultured epithelial cells (Supplementary Fig. 6E).

Interfaces between SipA and actin filament

The interface between the globular domain of SipA and the actin filament is unprecedented in that a single globular domain engages four actin subunits on the same strand (N+0, N+1, N+2, and N+3). SipA engages actin through hydrophobic interactions and ionic bonds (Fig. 3). Its interface with the actin N+0 subunit is relatively small (~155.3 $Å^2$), and it involves residues in the SD4 domain in actin and residues in helix 4 (H4) and loop 4 (L4) in $SipA_{447-685}$ (Fig. 3B and 3C, interface residues are highlighted in cyan). The interface between SipA and actin N+1 is the largest of all burying ~746.1 $Å^2$. This interface is stabilized by more substantial interactions involving residues in the SD1 and SD2 loops of the actin subunit and H1, L2, H2, L3, H3, L4, H4, and L5 in $SipA_{447-685}$ (Fig. 3B and 3C interface residues are highlighted in yellow). The interface between SipA and actin #N+2 is also substantial burying 531.6 $Å^2$ and involving acting residues mostly in the helices of SD3 and SD4 domain, engaging residues in L2, H1, L2, H2, L7, and H7 in $SipA_{446-684}$ (Fig. 3B and 3C, interface residues are highlighted in orange). Finally, the interface between SipA and actin #N+3 is mainly between the loops of SD1 and SD3 domain in actin and H2, L3, H7 and L8 in $SipA_{446-684}$ (Fig. 3B and 3C, interface residues are highlighted in green) and buries ~214.9 $Å^2$.

Overall, the combined interface between the globular domain of SipA and F-actin is very substantial thus explaining its rather high affinity for F-actin.

Comparison of SipA with other actin binding molecules

Because of their affinity for polymerized actin, the fungal toxins phalloidin and jasplakinolide are frequently used for visualizing filamentous actin. SipA targets actin at a similar site to where these fungal toxins bind filamentous actin (Fig. 4A). However, superimposition of the structures of SipA decorated actin with the toxin-actin complexes, revealed that the C-terminal extension domain of SipA would clash with the two toxins, indicating the binding of SipA may block the binding of phalloidin and jasplakinolide (Fig. 4A and 4B). Pyrene labeling has been widely employed to measure the kinetics of actin polymerization and the interaction between actin and actin-binding proteins including SipA (20, 29). In this context, it is of interest that SipA binds actin at a site very close to the pyrene-binding site (38) and that our structure shows that the binding of SipA alters the confirmation of the D-loop region in a manner that would interferes pyrene binding. More specifically, SipA binding to filamentous actin results in a conformational change in a tyrosine residue (Y143) located within the pyrene-binding site that is predicted to result in clashes with pyrene potentially interfering with its binding (Fig. 4C). Therefore, these observations suggest that SipA may affect actin polymerization assays that rely on pyrene-actin.

The SipA actin-binding site also overlaps with the binding site of other well characterized actin-regulatory proteins (Fig. 4). For example, SipA binds the same groove in F-actin that serves as a binding site for the muscle protein nebulin (Fig. 4D) (39) (40). Based on low resolution structures of SipA and Nebulin bound to actin, it was previously proposed that SipA mimics nebulin in its mechanism of actin-binding (30). Our structure is consistent with this notion since several actin residues engaged by SipA (e.g. K68, E117, E224, E276, and R372) are also engaged by nebulin (41).

The Arp2/3 complex are responsible for the formation of branches on actin filaments (42). Superimposition of our structure and the previous structure of the actin branch junction (PDB ID: 8E9B) (43) shows that SipA and Arp3 bind at the same site on actin filaments (Fig. 4E). Thus, binding of SipA likely inhibits the binding of Arp2/3 complex thus potentially preventing the branching of actin filaments.

It was previously reported that SipA interferes with the F-actin severing activity of ADF/cofilin (25). Although SipA and Cofilin (5YU8) (44) bind actin at different sites, superimposing the two structures showed that Cofilin clashes with the D-loop region and the C-terminal loop (S348-F352) of actin in the SipA-decorated filament (Fig. 4F). These observations provide a mechanistic explanation for the observation that F-actin filaments bound to SipA are resistant to the severing activity of ADF/cofilin (25).

Bacterial actin homologs lack structural features that are essential for SipA binding

Many bacteria, including *Salmonella*, encode highly conserved cytoskeletal proteins such as MreB and ParM that are structural homologs of actin (45, 46). However, despite the close structural similarities between mammalian actin and the bacterial counterparts, SipA should have evolved to be unable to target these bacterial actin homologs as such binding would likely be detrimental for bacterial physiology and could potentially trap SipA within the bacterial cytoplasm. Consistent with this notion, comparison of the structures of MreB and ParM with actin shows that several actin structural features that are crucial for the formation of its interface with SipA are partially or totally absent from MreB and ParM (Fig. 5). These results indicate that, as previously suggested (30), the SipA actin-binding sites have evolved to purposedly avoid binding to the bacterial actin homologs.

Structure-function analyses of SipA indicate that its actin-modulating and pro-inflammatory activities are independent from one another

SipA has been associated with two different phenotypes, bacterial invasion of intestinal epithelial cells through its actin-modulating activity (20), and the stimulation of intestinal inflammation through poorly understood mechanisms that involve its amino-terminal half (26, 27, 47). Whether the ability of SipA to stimulate intestinal inflammation requires its actin modulating activity is unclear since the lack of structural information has prevented the generation of a mutant specifically defective in this function while preserving the proper folding and integrity of the entire protein. This issue is pertinent since it has been shown that actin polymerization by itself, when triggered by microbial pathogens, can activate innate immune signaling (48). To address this issue, we introduced mutations in SipA residues that are implicated in the formation of its interface with actin and examined their effect on F-actin-binding and G-actin polymerization. Reflecting the redundant nature of the SipA-actin interface, none of the individual mutations introduced significantly affected the ability of SipA to bind actin. However, introduction of changes in 2 or more SipA residues involved in forming its interface with actin significantly reduced its binding affinity. Notably, simultaneous mutations in S537 and K636, which interact with the D-loop and C-terminus of actin, resulted in a drastic reduction in its binding affinity (Supplementary Fig. 7 and Fig. 6A).

To examine the contribution of the actin-binding activity of SipA in the interaction of *S.* Typhimurium with host cells, we constructed a mutant strain expressing the *sipA*$^{S537E/K636E}$ allele from its native chromosomal context. We then tested the resulting strain for its ability to stimulate actin-cytoskeletal rearrangements and invade cultured epithelial cells. We found that, in comparison to wild type, the actin cytoskeletal changes stimulated by the *S.* Typhimurium *sipA*$^{S537E/K636E}$ mutant strain were more restricted (Fig. 6B). Consistent with the more limited actin rearrangements, the invasion ability of the mutant strain was significantly impaired when measured with two independent assays (Fig. 6C-6E). Importantly, the phenotype of the *S.* Typhimurium *sipA*$^{S537E/K636E}$ mutant strain was indistinguishable from the phenotype of the S.

Typhimurium Δ*sipA* mutant, further demonstrating that the introduced mutations largely eliminated its ability to bind actin (Fig. 6C-6E).

To examine the potential contribution of the actin-modulating activity of SipA to stimulate inflammation, we compared the intestinal inflammatory response of mice that have been infected with wild-type *S*. Typhimurium, and isogenic mutants either lacking *sipA* or expressing the actin-binding defective mutant $SipA^{S536/K635}$. We found that after oral infection and as previously reported (27), the *S*. Typhimurium Δ*sipA* mutant strain was significantly impaired in its ability to stimulate intestinal inflammation. In contrast, the S. Typhimurium $sipA^{S536/K635}$ mutant strain exhibited significantly enhanced ability to stimulate intestinal inflammation compared to wild type (Fig. 6F). These results indicate that the actin-binding activity of SipA is not required to stimulate intestinal inflammation. In addition, the enhanced ability of the mutant strain to stimulate inflammation suggests that the two activities are not only independent from one another but that may be carried out by different SipA molecules operating independently on different targets.

Discussion

Bacterial effector proteins with the ability to modulate cellular processes are often evolutionary designed to mimic the activities of eukaryotic proteins that carry out a similar function (49, 50). This mimicry often involves convergent evolution since many of these bacterial mimics do not exhibit either primary sequence or structural similarity to their eukaryotic counterparts (49). The actin-binding effector protein SipA has been postulated to be a mimic of the actin-binding protein nebulin (30). In addition, it has been proposed to exert its actin-stabilizing function by working as a "molecular staple", making use of a carboxy terminal domain and two flexible arms to bind actin monomers on opposing actin strands (29). However, the lack of high-resolution structural information of SipA bound to actin filaments has prevented the rigorous testing of these hypotheses. To address these issues, we solved the cryo-EM structure of the actin-binding

carboxyterminal domain of SipA bound to actin. We found that SipA simultaneously engages 4 actin monomers through interactions largely involving its globular carboxy terminal domain. The SipA binding sites on actin overlap those of nebulin, a very large muscle skeletal protein, which through the tandem arrangement of multiple actin-binding domain repeats can engage up to 200 actin monomers (39). Our structure showed that SipA and nebulin bind the same groove in the actin filaments and share some of the actin residues necessary for their interaction. This observation therefore is consistent with the notion that SipA and the nebulin repeat exhibit a similar actin-binding mode.

Our structure also showed that the SipA actin-binding site also overlaps with the binding site of the well-characterized actin nucleator Arp2/3 complex. This observation has potential functional relevance since it suggests that SipA is likely to interfere with the binding of the Arp2/3 complex, thus potentially preventing the branching of SipA-stabilized actin filaments. However, more experiments will be required to test this hypothesis and to examine its potential functional significance.

It has been previously shown that SipA prevents the activity of the actin-severing proteins ADF/cofilin (25), thus further stabilizing SipA-bound actin filaments, which is thought to promote the formation of more pronounced ruffles. Our structure provides a mechanistic explanation for such activity. Although the actin-binding sites of SipA and ADF/Cofilin do not overlap, SipA binding triggers a conformational change in actin that disrupts the ADF/Cofilin binding site in a manner that leads to predicted structural clashes. The binding of cofilin to actin subunits drives a significant conformational change from a flattened to a twisted configuration. Residues in H4 and L3 of SipA bind to the D-loop of actin subunits and stabilize the flattened conformation, which would interfere with ADF/Cofilin binding.

Unlike what was observed in a previous low resolution cryo-EM structure of SipA bound to actin (29), our structure did not show the presence of non-globular arms engaging actin monomers on the opposite strand of the actin filaments and therefore could not confirm the

"molecular staple" model. However, an unstructured extension at the C-terminal end, which insert deep into the actin filament, was apparent in our structure. Furthermore, as previously shown, we found that this extension is required for the ability of SipA to increase the efficiency of bacterial invasion of cultured epithelial cells. Most likely, the contribution of this extension to bacterial invasion is related to SipA's role in facilitating the polimerization of G-actin but not to its ability to stabilize F-actin since removal of this extension altered the former but not the latter.

In addition to its ability to modulate actin dynamics to mediate bacterial invasion, SipA has been also implicated in the stimulation of intestinal inflammation (26, 27), which is critical for *S*. Typhimurium virulence (51). Although the mechanisms by which SipA modulates the inflammatory response are poorly understood, this activity has been largely correlated with its amino terminal domain (26, 27, 47). However, as the modulation of actin dynamics by bacterial pathogens has also been linked to the stimulation of innate immune responses involving inflammation (48), it has been unclear whether the carboxy terminal, actin-binding domain of SipA contributes to this phenotype. Indeed, the lack of structural information for the SipA-actin interface has hampered previous efforts to obtain a mutant that would specifically lack this activity without altering the overall structure of this effector protein (28). This issue is complicated by the redundant nature of the SipA-actin interface. In fact, a previously reported mutant utilized in a study to attempt to address this issue (28) in our hands retains the ability to modulate actin dynamics (Fig. 6). Using structurally guided mutagenesis we were able to identify a mutant that is specifically defective in actin binding without altering the overall conformation of SipA. As predicted by its inability to bind actin, an *S*. Typhimurium strain expressing this mutant stimulated more limited actin cytoskeleton rearrangements and was defective in bacterial invasion of cultured epithelial cells. In fact, these phenotypes were indistinguishable from those of a *S*. Typhimurium strain lacking *sipA*. To address the potential contribution of the actin-binding activity to the stimulation of intestinal inflammation, we tested the *S*. Typhimurium strain expressing the actin-binding defective SipA mutant for its ability to stimulate intestinal inflammation in a mouse model of infection. We found that,

surprisingly, the *S.* Typhimurium strain expressing the SipA mutant was able to stimulate increased inflammation in comparison to wild type. These results indicate that the actin-binding activity of SipA does not contribute to its ability to induce inflammation. In fact, the heightened inflammatory response triggered by the mutant defective in actin binding suggest that the two activities are not only independent but that may well compete with one another. It is likely that due to the high binding affinity, F-actin may act as a "sink", thus preventing a sub-pool of SipA from engaging in functions related to the stimulation of the inflammatory response. Therefore, the inability to bind actin may free more SipA molecules to carry out its inflammatory function.

Taken together, our structure function studies have revealed a unique mechanism by which a bacterial effector protein modulates actin dynamics. Indeed, its ability to bind four actin monomers with a single globular domain has not been previously reported for other actin-binding proteins. Furthermore, our studies have clarified the mechanism of action of this effector protein and provide unique insight into the *Salmonella* spp. virulence mechanisms.

Materials and Methods

Bacterial strains and growth conditions

The wild-type *Salmonella enterica* serovar Typhimurium SL1344 strain and its Δ*sipA* isogenic mutant have been previously described (20). The *S*. Typhimurium SL1344 derivative encoding $SipA^{S537E/K636E}$ was constructed by allelic exchange as previously described (52). All bacterial strains were cultured in L-Broth containing 0.3 M NaCl to an OD600 of 0.9, conditions that are known to stimulate the expression of the SPI-1 T3SS (53).

Plasmid construction, protein expression, and purification.

DNA manipulations were carried out using the standard Gibson assembly protocol (54). *S.* Typhimurium $SipA_{447-685}$ was expressed in a modified pQE vector with GST and a His_6 tags at its amino and carboxy terminal ends, respectively. $SipA_{447-685}$, $SipA_{498-659}$, and $SipA_{513-659}$, as well as $SipA_{447-685}$ carrying specific point mutations were expressed in *Escherichia coli* BL21 (DE3) and purified using affinity chromatography. Briefly, bacterial cells were cultured in LB medium at 37°C to an absorbance at OD_{600} of 0.8 to 1.0, induced with 0.2 mM isopropyl β-d-1-thiogalactopyranoside and grow for an additional 16 to 20 hs at 20°C. The bacteria were harvested by centrifugation and lysed using a One Shot cell disrupter following the manufacturer's instructions (Constant Systems Ltd., Daventry, United Kingdom). Cell lysates were cleared by centrifugation and the supernatant was loaded onto a Glutathione column. After elution, the GST tag was removed by digestion with HRV 3C protease. The digested protein mixture was further purified by passing through a second Glutathione column and a Ni^{2+}–nitrilotriacetic acid column.

Actin was purified as previously reported (55). Briefly, actin was purified from chicken muscle acetone powder which was made from flash-frozen chicken (purchased from a local Trader Joe's store). After one cycle of polymerization and depolymerization, G-actin was

isolated by gel filtration through Sephacryl S-300 in Ca-G-buffer (2 mM Tris·HCl, pH 8.0; 0.2 mM ATP; 0.1 mM CaCl2; 1 mM NaN3; 0.5 mM DTT).

Cell culture, bacterial infections, and visualization of the actin cytoskeleton

All cell lines were routinely tested for the presence of mycoplasma by a standard PCR method, checked for their morphological features, growth characteristics and functionalities, but were not authenticated by short tandem repeat profiling. The ability of *S*. Typhimurium strains to invade cultured human intestinal epithelial Henle-407 cells (obtained from the Roy Curtiss III collection in 1987) using the gentamicin protection assay was carried out as described previously (56). Briefly, ~24 hs after seeding onto tissue culture plates, cells were infected for the indicated time with the indicated *S*. Typhimurium strains with a m.o.i. of 20. Infected cells were washed and incubated for 2 hs in DMEM containing gentamicin (100 $\mu g\ ml^{-1}$) to kill extracellular bacteria. Alternatively, bacterial invasion was also measured using a differential staining protocol (inside-out staining) as described before (57). Briefly, cells were infected as indicated above and 20 min after infection, the cells were fixed in formalin and stained with rabbit anti-*Salmonella* lipopolysaccharide (LPS) antibody (SIFIN, catalog no.: TS 1624), followed by fluorescently labeled (Alexa Fluor 488) secondary anti-rabbit antibody. Cells were subsequently permeabilize with Triton X 100 (0.5 %) and stained with the anti-Salmonella LPS antibody followed by a fluorescently labeled (Alexa Fluor 594) anti-rabbit secondary antibody. In this protocol, extracellular bacteria are stained by both secondary antibodies while intracellular bacteria are only stained by the Alexa Fluor 594-labeled secondary antibody. Quantification of internalized bacteria was carried out by capturing a minimum of 30 fields per condition (containing a minimum of 1000 cells each) on a Nikon Eclipse inverted microscope equipped with an Andor's Zyla 5.5 sCMOS camera.

To visualize actin cytoskeleton rearrangements due to bacterial invasion, cells were infected, fixed, and permeabilized as indicated above and then stained with rhodamine-labeled

phalloidin (to visualize the actin cytoskeleton), an anti-*S.* Typhimurium LPS antibody (SIFIN, catalog no.: TS 1624), and Alexa Fluor 594 fluorescently labeled secondary antibody to visualize bacteria. Cells were visualized under an Andor Dragonfly spin disc fluorescence microscope (Oxford Scientific).

Mouse infections and measurement of intestinal inflammation

Groups of age- and sex-matched C57BL/6 mice were orally administered streptomycin (100 µl of 200 mg/ml solution) and 24 hs after antibiotic treatment were orally infected by stomach gavage with 10^7 cfu in 100 µl of PBS with the indicated strains. Three days after infection, feces were collected and the levels of lipocalin per 100 mg of feces, a measure of intestinal inflammation, were determined using a commercial kit (RayBiotech ELM-Lipocalin2-1) following the manufacturer's instructions. The sample sizes were empirically determined to optimize the numbers based on our previous experience with equivalent experiments. The mice were randomly assigned to the experimental groups, but experimenters were not blind to the assignment.

EM sample preparation, data acquisition, and image processing

Purified G-actin was first polymerized in KMEI buffer (50 mM KCl, 1 mM MgCl2, 1 mM EGTA and 10 mM Imidazole pH 7.5) for 20 min, followed by the addition of SipA with a molar ratio of 1.7:1. The CapZ protein was added into the polymerized actin filaments with a molar ratio of 1:30 to avoid the formation of long and bundled actin filaments.

For negative staining, actin filaments or SipA decorated actin filaments were applied onto glow-discharged carbon-coated grids and negatively stained with 0.8% (wt/vol) uranyl formate. Images were collected using a Talos L120C electron Microscope (Thermo Fisher) operating at 120 kV.

For cryo-EM analysis, 3 µl of sample were deposited onto glow-discharged Quantifoil R2/1 300 Mesh Gold Holey Carbon Grids (SPI supplies) and plunged into liquid ethane using a Vitrobot

Mark IV (Thermo Fisher) at 10°C and 100% humidity. The freezing conditions were screened on a Glacios cryo TEM (Thermo Fisher) operating at 200 kV. Cryo-EM data collection was performed using a Titan Krios electron microscope (Thermo Fisher) equipped with a K3 direct electron detector (Gatan) operating at 300 kV. Data were collected at a calibrated magnification of 81,000 x (1.068 Å per pixel) in super resolution mode, with defocus values between −2.5 μm and −1.2 μm. Images were recorded using the beam image shift implemented in SerialEM (58). Forty-four frames were taken at 0.05s per frame, with a dose rate of 29 e− per pixel per s. In total 4740 movies were recorded with an exposure time of 2.2 s. Motion correction and contrast transfer function (CTF) estimation were done using Relion 4.0 (59). Particles were manually picked by using sxhelixboxer.py in SPARX (60). Layer-line images were calculated with SPARX (project and periodogram commands) (Supplementary Fig. 8,) In total, 320,109 particle segmentations were boxed out from 2,370 images and subjected to further 2D and 3D calculations in Relion 4.0. The cryo-EM structure of ADP-Pi-Actin (EMDB accession number: 7937) was used as the initial model (rise: 110 Å and twist: 53.2 ^{O}) were imposed on the reconstruction. Due to the low map occupancy of SipA, a local map enhancement approach (DeepEMhancer) (33) was used to improve map visibility and connectivity. The final map has a global nominal resolution of 3.6 Å (based on the FSC using the 0.143 criterion). All the structural calculations were carried out on the Yale High Performance Computing servers.

Model Building and refinement.

The cryo-EM structure of ADP-Actin (PDB ID: 6DJON) (38) and crystal structure of SipA (PDB ID: 1Q5Z) (29) were used as initial templates to dock into the EM density maps using Chimera (35). The modeled structure was manually adjusted in Coot (61) and refined with Phenix (62). The SipA-actin interfaces was calculated with PDBePISA (63). Figures were generated using Coot, PyMOL, and Chimera.

Actin co-sedimentation assay.

To test the binding affinity of the different SipA mutants, actin monomers were first polymerized into filaments in KMEI buffer (50 mM KCl, 1 mM MgCl2, 1 mM EGTA and 10 mM Imidazole pH 7.5) for 20 min. Then different concentrations (0, 1, 2, 3, 4, and 10 μM) of polymerized actin filaments were incubated with 4 μM of SipA for 10 min at room temperature. Followed by ultracentrifugation at 120,000 × g in a TL100 rotor (Beckman Instruments, Fullerton, CA) at 4°C for 30 min, equal amount of the supernatant from every reaction were loaded onto SDS–PAGE Gel and stained with Coomassie blue.

To test the actin nucleation activity of $SipA_{447-685}$, $SipA_{498-659}$, and $SipA_{513-659}$, the SipA proteins were first dialyzed against a Tris buffer without salt (25 mM Tris, pH 7.5) three times before adding to G actin. After 4 h incubation, the samples were ultracentrifuged at 120,000 × g in a TL100 rotor (Beckman Instruments, Fullerton, CA) at 4°C for 30 min, then equal amount of the supernatant and pellet from every reaction were loaded onto SDS–PAGE Gel and stained with Coomassie blue.

Data Availability.

The EM maps and atomic coordinates have been deposited in Electron Microscopy Data Bank (EMDB) under accession number EMD-42017 and Protein Data Bank (PDB) under accession code 8U88.

Ethics statement

All animal experiments were conducted according to protocols approved by Yale University's Institutional Animal Care and Use Committee (IACUC) under protocol number 2022–07858. The IACUC is governed by applicable Federal and State regulations, including those of the Animal Welfare Act, Public Health Service and the United States Department of Agriculture and is guided

by the US Government Principles for the Utilization and Care of Vertebrate Animals Used in Testing, Research and Training.

Acknowledgements

We thank Dr. Jianfeng Lin, Dr. Shenping Wu, Dr. Marc Llaguno, and Dr. Xinran Liu for managing the microscope resources, the Yale High Performance Computing support team for guidance and use of the computing infrastructure. We also thank Florian Schueder for assistance in the imaging of the actin cytoskeleton rearrangements induced by the different *S*. Typhimurium strains. This work was supported by a NIH Grant R01AI055472 to J. E. G.

References

1. A. Voetsch *et al.*, FoodNet estimate of the burden of illness caused by nontyphoidal Salmonella infections in the United States. *Clin Infect Dis.* **38**, S127-134 (2004).
2. C. Parry, E. Threlfall, Antimicrobial resistance in typhoidal and nontyphoidal salmonellae. *Curr Opin Infect Dis.* **21**, 531-538 (2008).
3. J. Crump, E. Mintz, Global trends in typhoid and paratyphoid Fever. *Clin Infect Dis.* **50**, 241-246 (2010).
4. M. E. Ohl, S. I. Miller, Salmonella: a model for bacterial pathogenesis. *Annu. Rev. Med.* **52**, 259-274. (2001).
5. G. Grassl, B. Finlay, Pathogenesis of enteric Salmonella infections. *Curr Opin Gastroenterol.* **24**, 22-26 (2008).
6. C. Parry, T. T. Hien, G. Dougan, N. White, J. Farrar, Typhoid fever. *N Engl J Med.* **347**, 1770-1782 (2002).
7. M. Raffatellu, R. Wilson, S. Winter, A. Bäumler, Clinical pathogenesis of typhoid fever. *J Infect Dev Ctries* **2**, 260-266 (2008).
8. G. Dougan, S. Baker, Salmonella enterica serovar Typhi and the pathogenesis of typhoid fever. *Annu Rev Microbiol.* **68**, 317-336 (2014).
9. J. E. Galán, Salmonella interaction with host cells: Type III Secretion at Work. *Annu. Rev. Cell Dev. Biol.* **17**, 53-86 (2001).
10. D. LaRock, A. Chaudhary, S. Miller, Salmonellae interactions with host processes. *Nat Rev Microbiol.* **13**, 191-205 (2015).
11. P. Hume, V. Singh, A. Davidson, V. Koronakis, Swiss Army Pathogen: The Salmonella Entry Toolkit. *Front Cell Infect Microbiol.* **7**, 348-358 (2017).
12. S. Fattinger, M. Sellin, W. Hardt, Salmonella effector driven invasion of the gut epithelium: breaking in and setting the house on fire. *Curr Opin Microbiol.* **64**, 9-18 (2021).
13. W.-D. Hardt, L.-M. Chen, K. E. Schuebel, X. R. Bustelo, J. E. Galán, *Salmonella typhimurium* encodes an activator of Rho GTPases that induces membrane ruffling and nuclear responses in host cells. *Cell* **93**, 815-826 (1998).
14. C. Bakshi *et al.*, Identification of SopE2, a Salmonella secreted protein which is highly homologous to SopE and involved in bacterial invasion of epithelial cells. *J. Bacteriol.* **182**, 2341-2344 (2000).
15. J. C. Patel, J. E. Galan, Differential activation and function of Rho GTPases during Salmonella-host cell interactions. *J Cell Biol* **175**, 453-463 (2006).
16. D. Zhou, L. M. Chen, L. Hernandez, S. B. Shears, J. E. Galan, A Salmonella inositol polyphosphatase acts in conjunction with other bacterial effectors to promote host cell actin cytoskeleton rearrangements and bacterial internalization. *Mol Microbiol* **39**, 248-259 (2001).
17. D. Humphreys, A. Davidson, P. Hume, V. Koronakis, Salmonella virulence effector SopE and Host GEF ARNO cooperate to recruit and activate WAVE to trigger bacterial invasion. *Cell Host Microbe.* **11**, 129-139 (2012).

18. A. Criss, J. Casanova, Coordinate regulation of Salmonella enterica serovar Typhimurium invasion of epithelial cells by the Arp2/3 complex and Rho GTPases. *Infect Immun.* **71**, 2885-2891 (2003).
19. S. Stender *et al.*, Identification of SopE2 from Salmonella typhimurium, a conserved guanine nucleotide exchange factor for Cdc42 of the host cell. *Mol Microbiol.* **36**, 1206-1211. (2000).
20. D. Zhou, M. Mooseker, J. E. Galán, Role of the *S. typhimurium* actin-binding protein SipA in bacterial internalization. *Science* **283**, 2092-2095 (1999).
21. R. D. Hayward, V. Koronakis, Direct nucleation and bundling of actin by the SipC protein of invasive Salmonella. *EMBO J.* **18**, 4926-4934. (1999).
22. C. Collazo, J. E. Galán, The invasion-associated type III system of *Salmonella typhimurium* directs the translocation of Sip proteins into the host cell. *Mol. Microbiol.* **24**, 747-756 (1997).
23. J. Chang, J. Chen, D. Zhou, Delineation and characterization of the actin nucleation and effector translocation activities of Salmonella SipC. *Mol Microbiol.* **55(**1379-1389 (2005).
24. E. McGhie, R. Hayward, V. Koronakis, Cooperation between actin-binding proteins of invasive Salmonella: SipA potentiates SipC nucleation and bundling of actin. *EMBO J.* **20**, 2131-2139 (2001).
25. McGhie EJ, Hayward RD, K. V., Control of actin turnover by a salmonella invasion protein. *Mol Cell.* **13**, 497-510 (2004).
26. Wall DM *et al.*, Identification of the Salmonella enterica serotype typhimurium SipA domain responsible for inducing neutrophil recruitment across the intestinal epithelium. *Cell Microbiol.* **9**, 2299-2313 (2007).
27. S. Hapfelmeier *et al.*, Role of the Salmonella pathogenicity island 1 effector proteins SipA, SopB, SopE, and SopE2 in Salmonella enterica subspecies 1 serovar Typhimurium colitis in streptomycin-pretreated mice. *Infect Immun.* **72**, 795-809 (2004).
28. D. Li, X. Wang, L. Wang, D. Zhou, The actin-polymerizing activity of SipA is not essential for Salmonella enterica serovar Typhimurium-induced mucosal inflammation. *Infect Immun.* **81**, 1541-1549 (2013).
29. M. Lilic *et al.*, Salmonella SipA polymerizes actin by stapling filaments with nonglobular protein arms. *Science* **301**, 1918-1921. (2003).
30. V. E. Galkin *et al.*, The bacterial protein SipA polymerizes G-actin and mimics muscle nebulin. *Nat Struct. Biol.* **9**, 518-521. (2002).
31. J. Jumper *et al.*, Highly accurate protein structure prediction with AlphaFold. *Nature* **596**, 583-589 (2021).
32. R. Evans *et al.*, Protein complex prediction with AlphaFold-Multimer. *bioRxiv* 10.1101/2021.10.04.463034, 2021.2010.2004.463034 (2021).
33. R. Sanchez-Garcia *et al.*, DeepEMhancer: a deep learning solution for cryo-EM volume post-processing. *Commun Biol.* **4**, 874 (2021).
34. S. Chou, T. Pollard, Mechanism of actin polymerization revealed by cryo-EM structures of actin filaments with three different bound nucleotides. *Proc Natl Acad Sci U S A.* **116**, 4265-4274 (2019).
35. T. Goddard *et al.*, UCSF ChimeraX: Meeting modern challenges in visualization and analysis. *Protein Sci.* **27**, 14-25 (2018).

36. P. Emsley, K. Cowtan, Coot: model-building tools for molecular graphics. *Acta Crystallogr.* **D 60**, 2126–2132 (2004).
37. P. Adams *et al.*, PHENIX: a comprehensive Python-based system for macromolecular structure solution. *Acta Cryst.* **D66**, 213-221 (2010).
38. S. Chou, T. Pollard, Cryo-electron microscopy structures of pyrene-labeled ADP-Pi- and ADP-actin filaments. *Nat Commun.* **11**, 5897 (2020).
39. M. Yuen, C. A. C. Ottenheijm, Nebulin: big protein with big responsibilities. *J Muscle Res Cell Motil* **41**, 103-124 (2020).
40. Z. Wang *et al.*, Structures from intact myofibrils reveal mechanism of thin filament regulation through nebulin. *Science* **375**, eabn1934 (2022).
41. Z. Wang *et al.*, Structures from intact myofibrils reveal mechanism of thin filament regulation through nebulin. *375* **375**, eabn1934 (2022).
42. P. Bieling, K. Rottner, From WRC to Arp2/3: Collective molecular mechanisms of branched actin network assembly. *Curr Opin Cell Biol.* **80**, 102156 (2023).
43. S. Chou, M. Chatterjee, T. Pollard, Mechanism of actin filament branch formation by Arp2/3 complex revealed by a high-resolution cryo-EM structureof the branch junction. *Proc Natl Acad Sci U S A.* **119**, e2206722119 (2022).
44. K. Tanaka *et al.*, Structural basis for cofilin binding and actin filament disassembly. *Nat Commun.* **9**, 1860 (2018).
45. J. Shaevitz, Z. Gitai, The structure and function of bacterial actin homologs. *Cold Spring Harb Perspect Biol.* **2**, a000364 (2010).
46. E. Ozyamak, J. Kollman, A. Komeili, Bacterial actins and their diversity. *Biochemistry* **52**, 6928-6939 (2013).
47. M. Raffatellu *et al.*, SipA, SopA, SopB, SopD, and SopE2 contribute to Salmonella enterica serotype typhimurium invasion of epithelial cells. *Infect Immun* **73**, 146-154 (2005).
48. S. Ahrens *et al.*, F-actin is an evolutionarily conserved damage-associated molecular pattern recognized by DNGR-1, a receptor for dead cells. *Immunity* **36**, 635-645 (2012).
49. C. E. Stebbins, J. E. Galan, Structural mimicry in bacterial virulence. *Nature* **412**, 701-705 (2001).
50. N. Elde, H. Malik, The evolutionary conundrum of pathogen mimicry. *Nat Rev Microbiol.* **7**, 787-797 (2009).
51. J. Galan, Salmonella Typhimurium and inflammation: a pathogen-centric affair. *Nat. Rev. Microbiol.* **19**, 716–725 (2021).
52. K. Kaniga, J. C. Bossio, J. E. Galan, The Salmonella typhimurium invasion genes invF and invG encode homologues of the AraC and PulD family of proteins. *Mol Microbiol* **13**, 555-568 (1994).
53. J. E. Galán, R. Curtiss III, Expression of *Salmonella typhimurium* genes required for invasion is regulated by changes in DNA supercoiling. *Infect. Immun.* **58**, 1879-1885 (1990).
54. D. G. Gibson *et al.*, Enzymatic assembly of DNA molecules up to several hundred kilobases. *Nat Methods* **6**, 343-345 (2009).

55. S. Z. Chou, T. D. Pollard, Mechanism of actin polymerization revealed by cryo-EM structures of actin filaments with three different bound nucleotides. *Proc Natl Acad Sci U S A* **116**, 4265-4274 (2019).
56. J. E. Galán, R. Curtiss III, Cloning and molecular characterization of genes whose products allow *Salmonella typhimurium* to penetrate tissue culture cells. *Proc. Natl. Acad. Sc. USA* **86**, 6383-6387 (1989).
57. L. M. Chen, S. Hobbie, J. E. Galan, Requirement of CDC42 for Salmonella-induced cytoskeletal and nuclear responses. *Science* **274**, 2115-2118 (1996).
58. D. Mastronarde, Automated electron microscope tomography using robust prediction of specimen movements. *J Struct Biol.* **152**, 36-51 (2005).
59. D. Kimanius, L. Dong, G. Sharov, T. Nakane, S. H. W. Scheres, New tools for automated cryo-EM single-particle analysis in RELION-4.0. *Biochem J* **478**, 4169-4185 (2021).
60. M. Hohn *et al.*, SPARX, a new environment for Cryo-EM image processing. *J Struct Biol* **157**, 47-55 (2007).
61. P. Emsley, B. Lohkamp, W. G. Scott, K. Cowtan, Features and development of Coot. *Acta Crystallogr D Biol Crystallogr* **66**, 486-501 (2010).
62. P. V. Afonine *et al.*, Real-space refinement in PHENIX for cryo-EM and crystallography. *Acta Crystallogr D Struct Biol* **74**, 531-544 (2018).
63. E. Krissinel, K. Henrick, Inference of macromolecular assemblies from crystalline state. *J. Mol.Biol.* **372**, 774–797 (2007).

Figure legends:

Figure 1. Overall structure of SipA$_{447-685}$-decorated actin filaments. Side views of SipA$_{447-685}$ decorated actin filaments. SipA$_{446-684}$ subunits are colored in magenta and actin subunits are colored in different shades of greens.

Figure 2. Atomic model of SipA$_{446-684}$-decorated actin filament. (**A**) Ribbon diagram model of SipA$_{446-684}$-decorated actin filaments. SipA is shown in magenta and actin in green. (**B**) Alignment of the globular domain of SipA when bound to actin (magenta) with its crystal structure in solution (PDB ID: 1Q5Z) (yellow). (**C**) Superimposition of the structure of actin when bound to SipA with the structure of ADP-Pi-actin (PDB ID: 6DJON). The D loop region is denoted by a box.

Figure 3. SipA interacts with four actin subunits. (**A**) Ribbon diagram model showing that one SipA subunit (magenta) interacts with four actin subunits (actin subunit N, cyan; actin subunit N+1, yellow; actin subunit N+2, orange; actin subunit N+3, green). (**B**) Ribbon representation of the structure of an actin subunit depicting its SipA-interacting surfaces. The different domains are labeled (SD1, SD2, SD3, and SD4) and the residues located at the different SipA interfaces are highlighted following the same color scheme as in (**A**). (**C**) Ribbon representation of the structure of SipA$_{446-684}$ depicting its actin-interacting surfaces. The different secondary structure elements are labeled, and residues located at different actin-interfaces are highlighted following the same color scheme as in (**A**).

Figure 4. Comparison of SipA with other actin binding molecules. (**A-C**) Superimposition of the structures of SipA and Phalloidin (PDB ID: 7BTI) (**A**), Jasplakinolide (PDB ID: 6T23) (**B**), or Pyrene (PDB ID: 7K20) (**C**) bound to actin. Structure of Nebulin (PDB ID: 7QIM) bound to actin

filaments showing the overlap with the SipA-binding sites. (**D**) Structure of Arp2/3 complex bound to actin filament (PDB ID: 8E9B) depicting the overlap with the SipA-binding sites. (**E**) Depiction of the Cofilin clashes with the D-loop region and the C-terminal loop (S348-F352) of actin after binding to SipA. SipA, magenta; actin filament, light gray; Phalloidin, green; Jasplakinolide, yellow; Nebulin,cyan; Arp2/3 complex, orange; Cofilin, blue

Figure 5. SipA binding sites are absent from the bacterial actin homologs MreB and ParM. Alignment of the atomic structures of MreB (light orange) (**A**) or ParM (light purple) (**B**) with the structure of actin as it appears bound to SipA (white). Residues located at different SipA-actin interfaces are highlighted following the same color scheme as in figure 3B. The loops and helices that are not present in ParM or MreB but located at the SipA-actin interfaces are highlighted.

Figure 6. Structure-function analysis of the SipA-actin interface. (**A**) Binding affinity of different SipA mutants in residues predicted to form its interface with actin as determined by a co-sedimentation assay. Bar graph shows the actin binding affinities of the indicated $SipA_{447-685}$ mutant proteins and values are the result of three independent experiments. Black dots indicate the values from each individual experiment and the standard deviations (two tailed Student *t* test) are shown. (**B**) Actin cytoskeletal rearrangements observed after infection with (as indicated) wild type *S*. Typhimurium, a Δ*sipA* isogenic mutant, and a strain expressing the $SipA^{S537E/K636E}$ mutant, which is defective for actin-binding. Actin was stained with rhodamine-labeled phalloidin (magenta) and bacteria were stained with an antibody directed to the *S*. Typhimurium LPS (green). (**C**-**E**) Cultured epithelial cell invasion ability of *S*. Typhimurium strain expressing a SipA mutant ($SipA^{S537E/K636E}$), which is unable to bind actin. The invasive ability of the different strains was measure by the gentamicin protection (**C**), or the differential (inside-out) staining (**D** and **E**) assays. Values in (**C**) represent the percentage of the inoculum that survived antibiotic treatment due to internalization and are the mean ± SD (two tailed Student *t* test) of six independent

experiments normalized to wild type, which was set to 1. (***: P<0.001; ****: P<0.0001) w. t.: wild type. Representative fluorescence microscopy images of *S.* Typhimurium after staining of nonpermeabilized (red) or permeabilized (green) infected cultured epithelial cells are shown in (**E**). The quantification of internalized bacteria by the differential staining assay is shown in (**D**). Values represent mean ± SD of the ratio of internalized vs total bacteria derived from the quantification of a minimum of 1,000 cells per condition in three different experiments. (*: P<0.05; **: P<0.01, two tailed Student *t* test). w. t.: wild type.

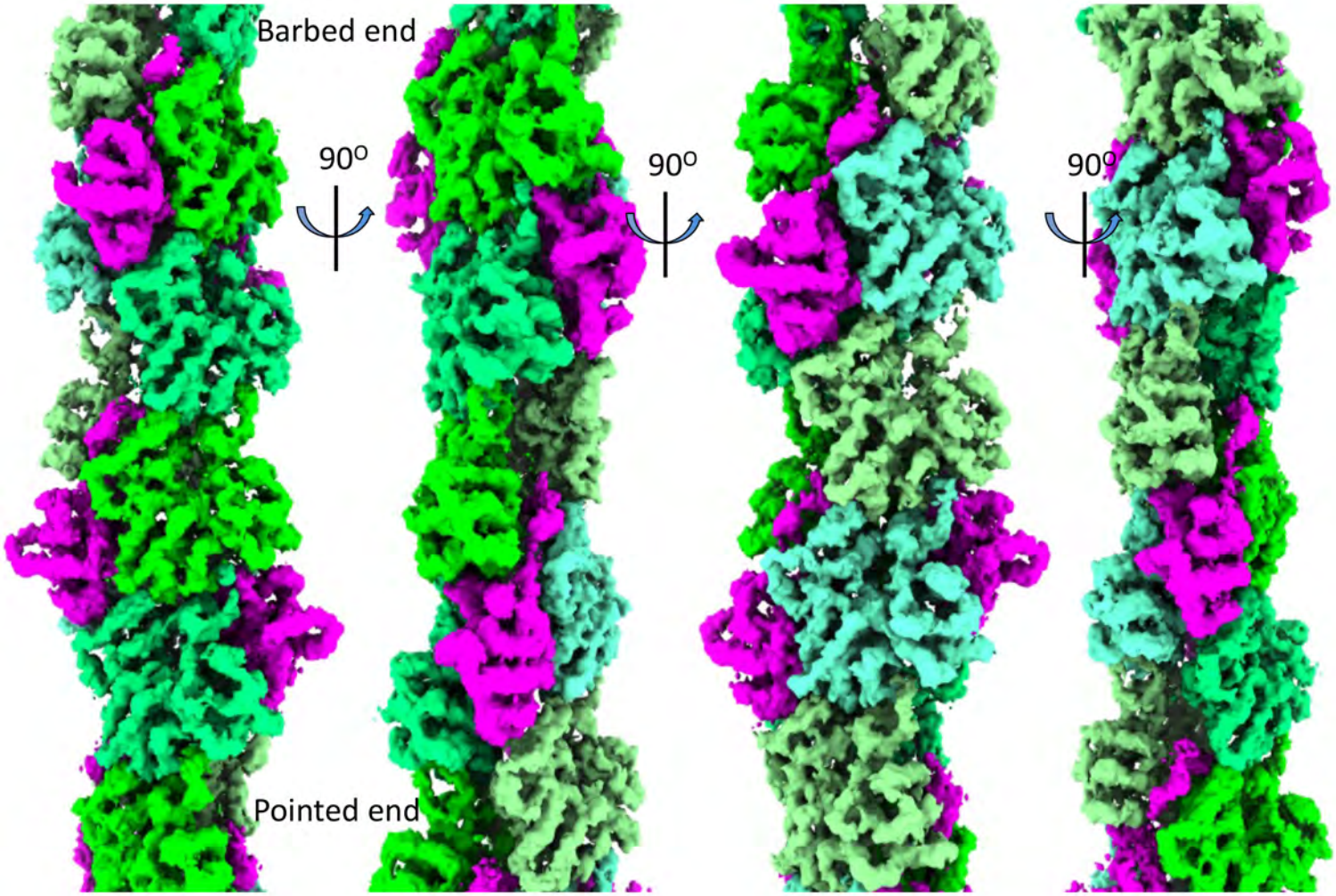

Figure 1

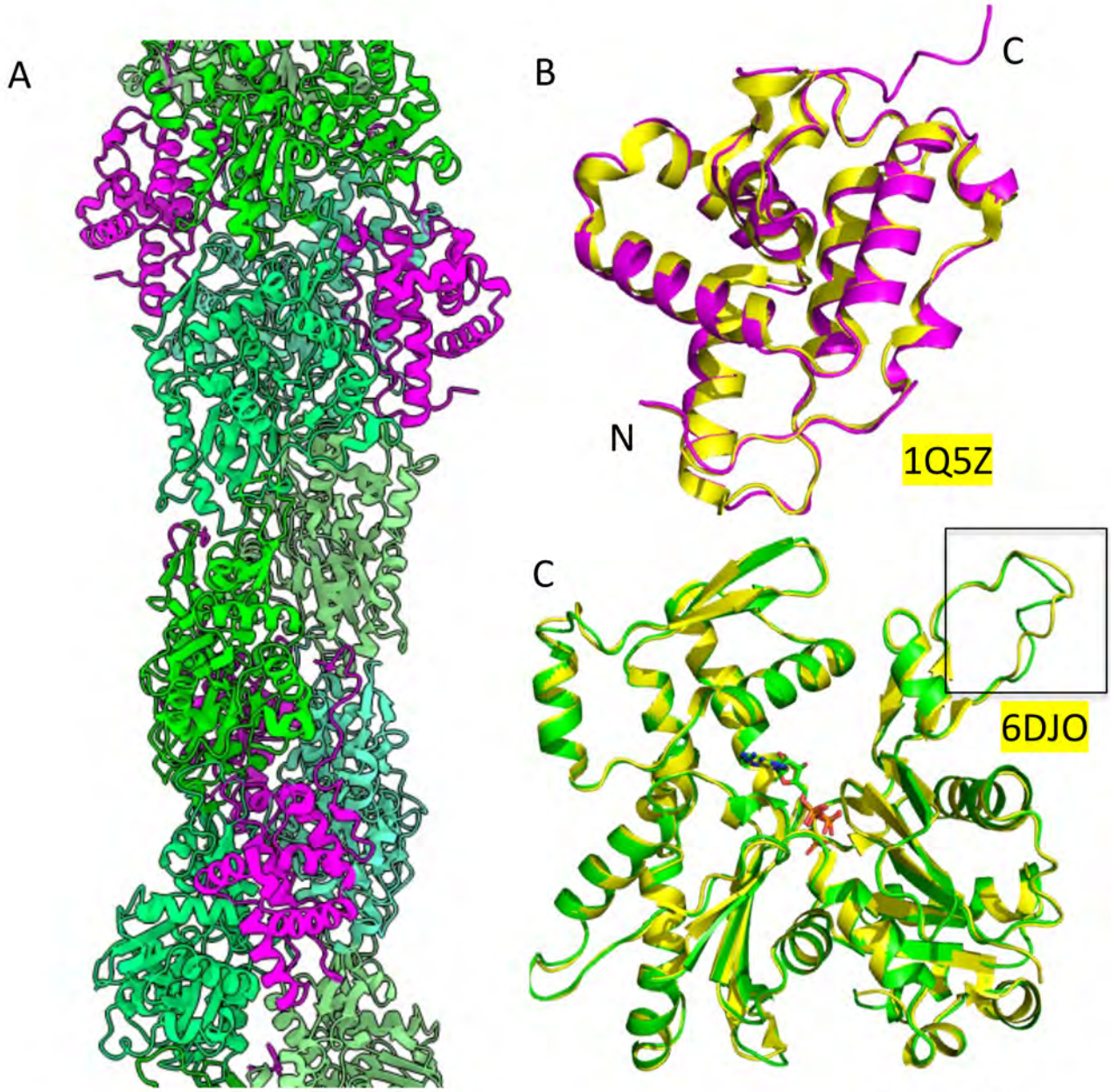

Figure 2

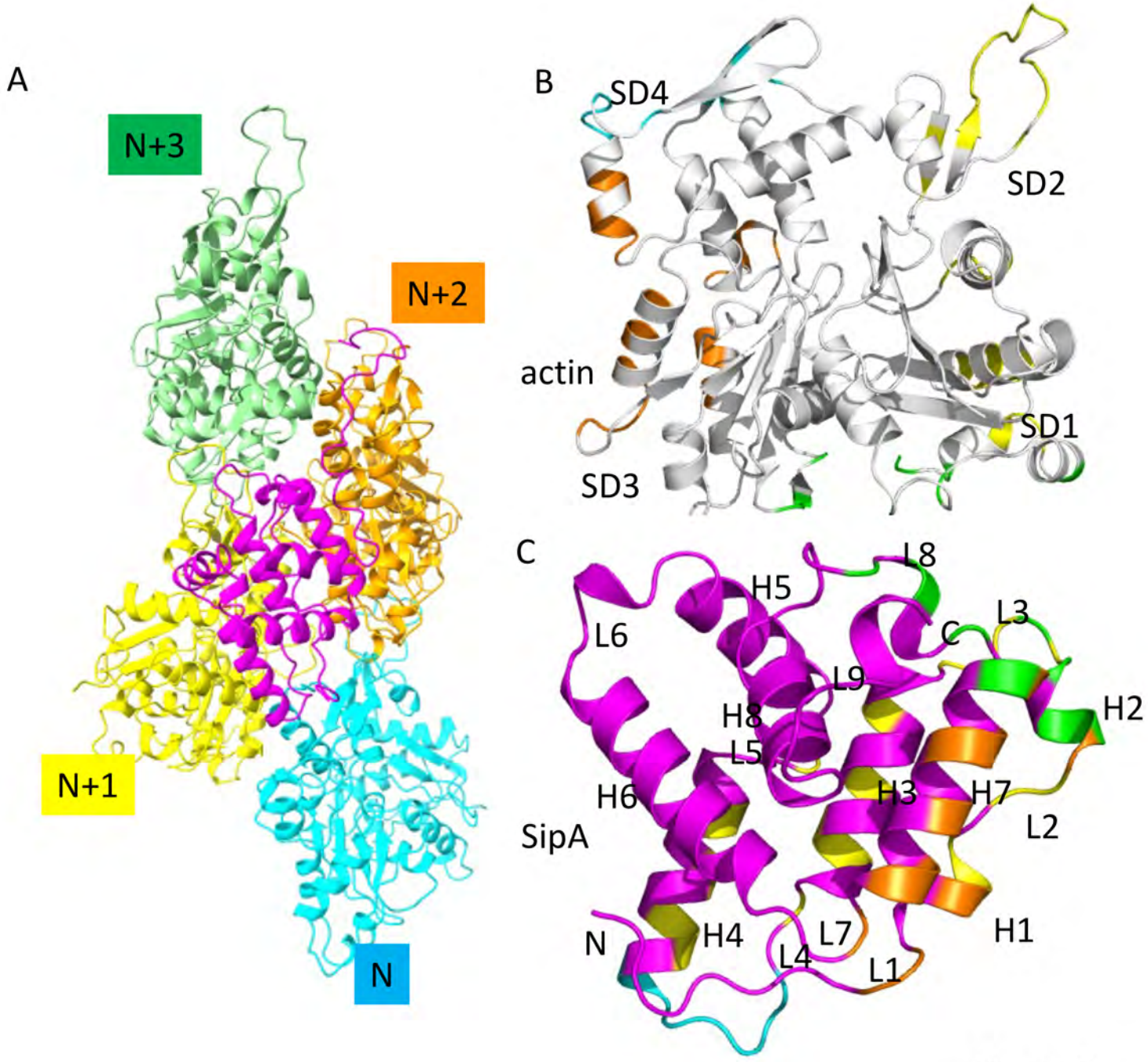
A
N+3
N+2
N+1
N
B
SD4
SD2
actin
SD1
SD3
C
L8
H5
L3
L6
C
L9
H2
H8
L5
H6
H3
H7
SipA
L2
N
H4
L7
H1
L4
L1

Figure 3

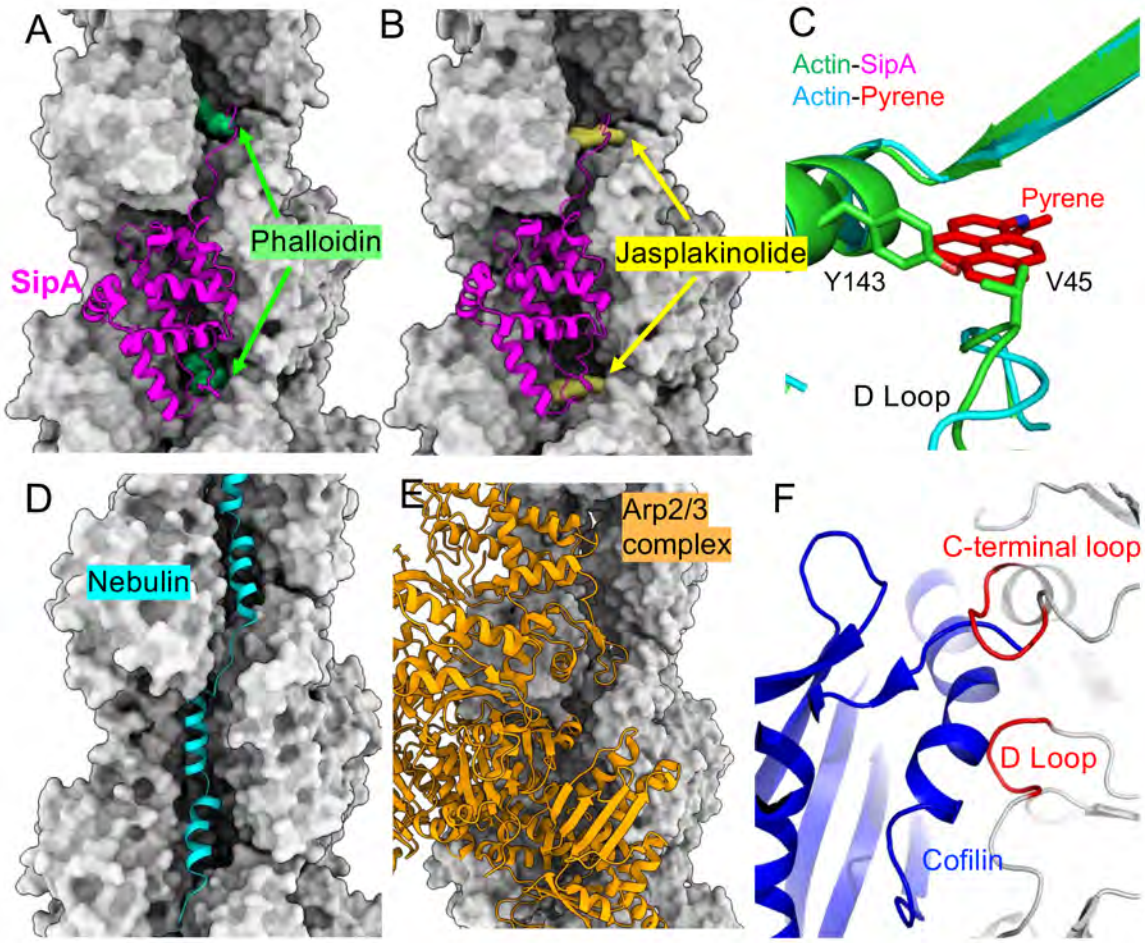
A
B
C
Actin-SipA
Actin-Pyrene
Phalloidin
SipA
Jasplakinolide
Pyrene
Y143
V45
D Loop
D
E
F
Nebulin
Arp2/3
complex
C-terminal loop
D Loop
Cofilin

Figure 4

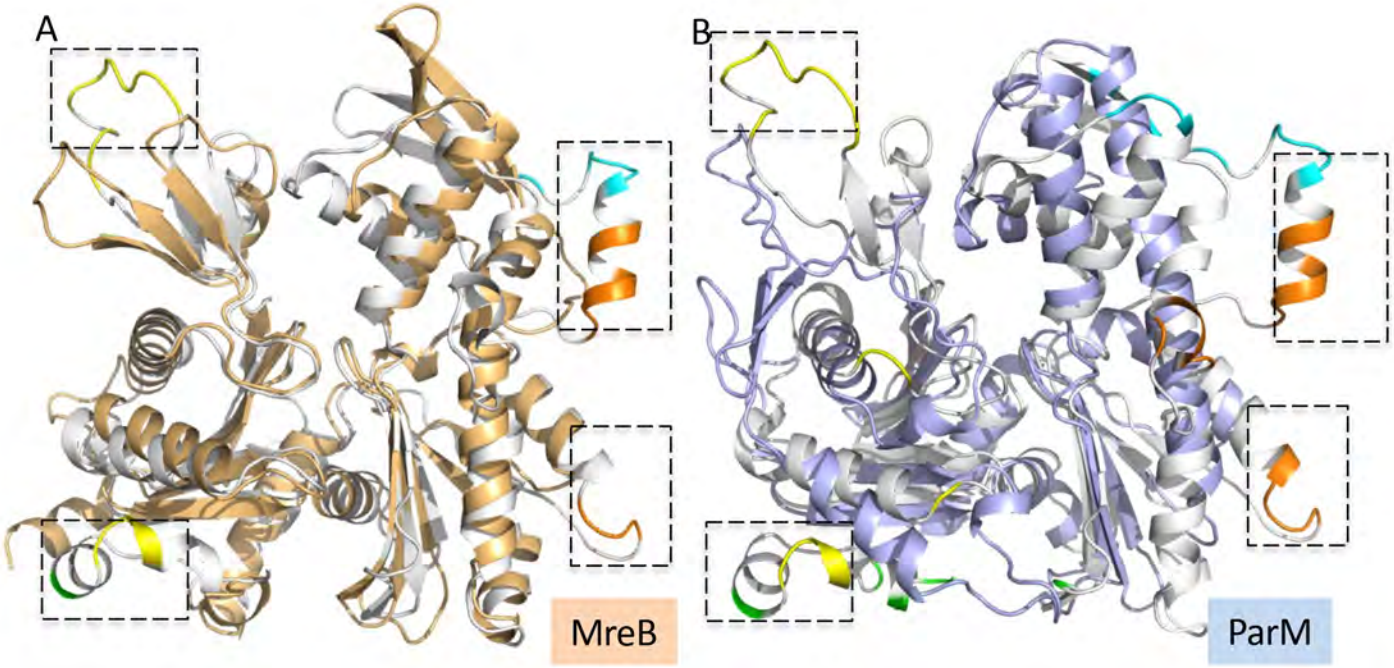

Figure 5

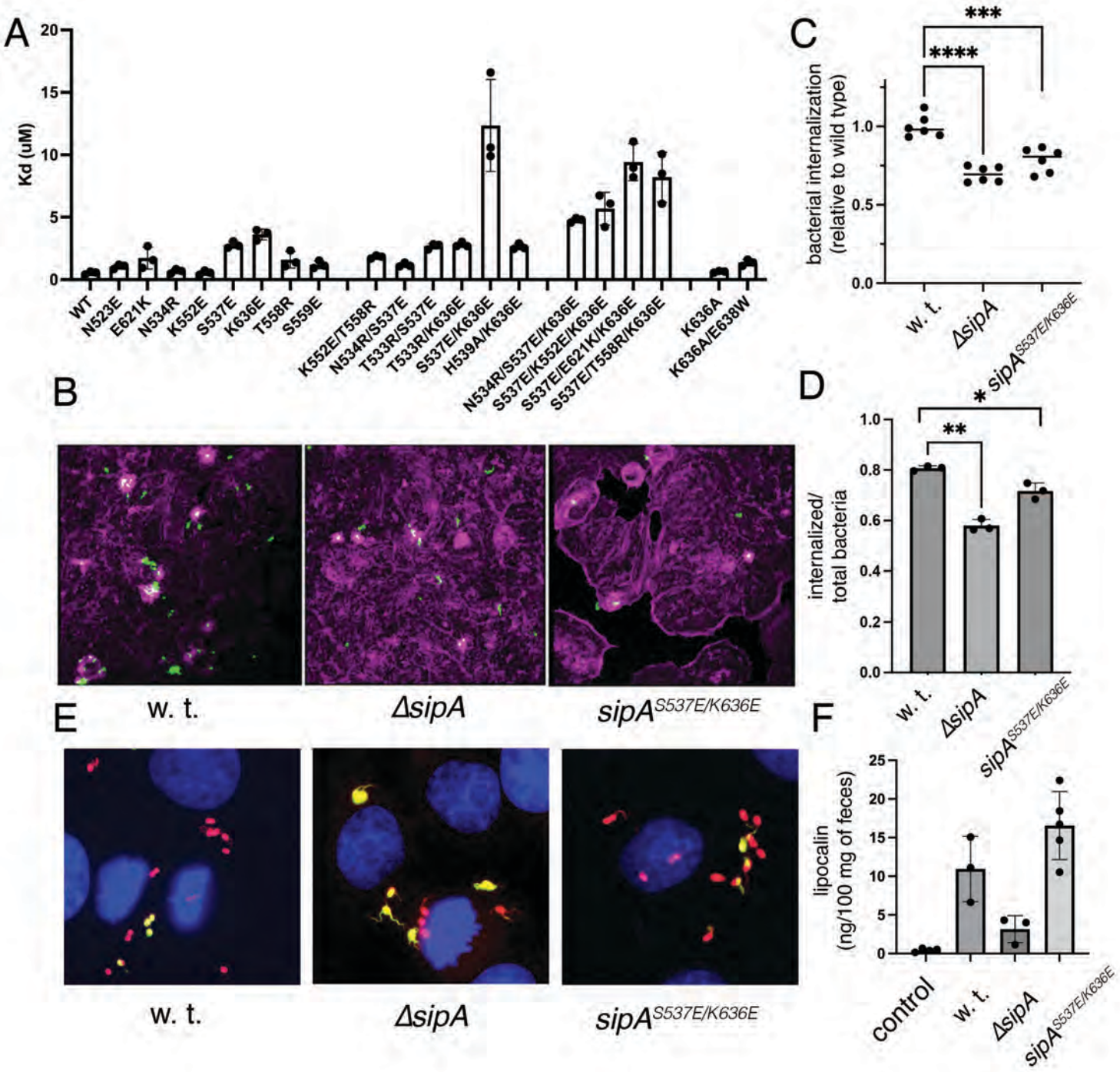
A
Kd (uM)
20
15
10
5
0
WT
N523E
E621K
N534R
K552E
S537E
K636E
T558R
S559E
K552E/T558R
N534R/S537E
T533R/S537E
T533R/K636E
S537E/K636E
H539A/K636E
N534R/S537E/K636E
S537E/K552E/K636E
S537E/E621K/K636E
S537E/T558R/K636E
K636A
K636A/E638W
C
***
****
bacterial internalization
(relative to wild type)
1.0
0.5
0.0
w. t.
ΔsipA
sipA S537E/K636E
B
w. t.
ΔsipA
sipA S537E/K636E
D
*
**
internalized/
total bacteria
1.0
0.8
0.6
0.4
0.2
0.0
w. t.
ΔsipA
sipA S537E/K636E
E
w. t.
ΔsipA
sipA S537E/K636E
F
lipocalin
(ng/100 mg of feces)
25
20
15
10
5
0
control
w. t.
ΔsipA
sipA S537E/K636E

Figure 6

Supplementary Figures for:

Cryo-EM structure of the bacterial effector protein SipA bound to F-actin reveals a unique mechanism for filament stabilization

Emily Guo[1], Steven Z. Chou[2], Maria Lara-Tejero[1], and Jorge E. Galán[1]*

[1]Department of Microbial Pathogenesis, Yale University School of Medicine, New Haven, CT 06536, and [2]Department of Molecular Biology and Biophysics, UConn Health, Farmington, CT 06030

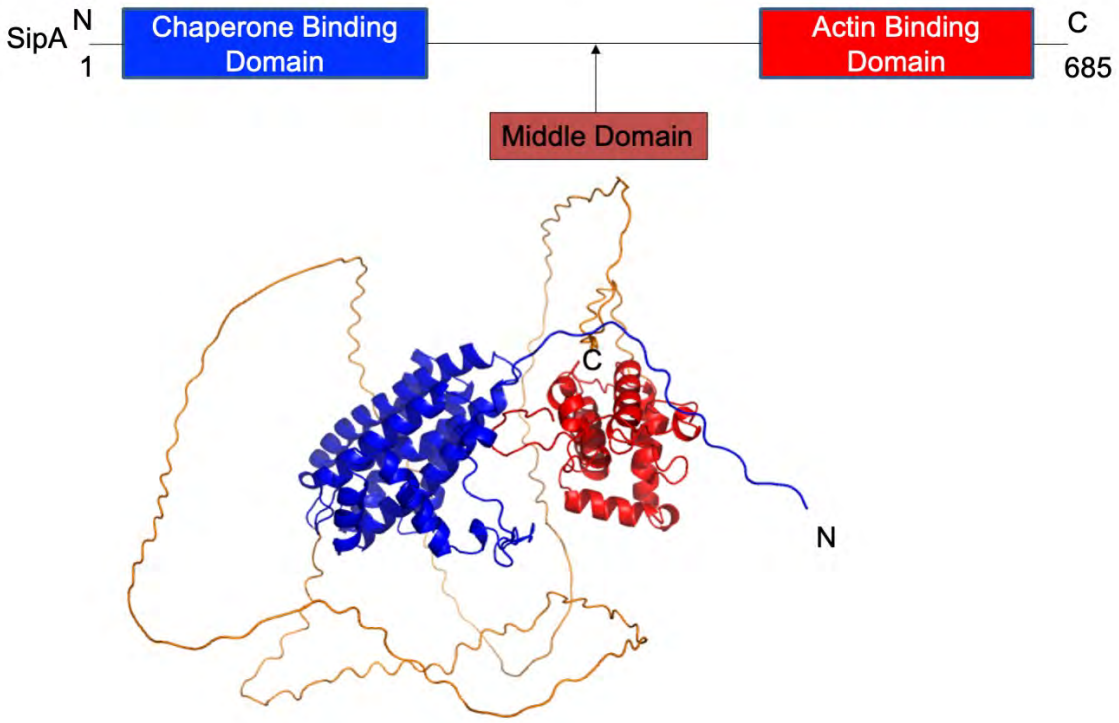

Supplementary Fig. 1. Diagram of the SipA S. Typhimurium effector protein. The AlphaFold prediction of the structure of the SipA monomer is also shown.

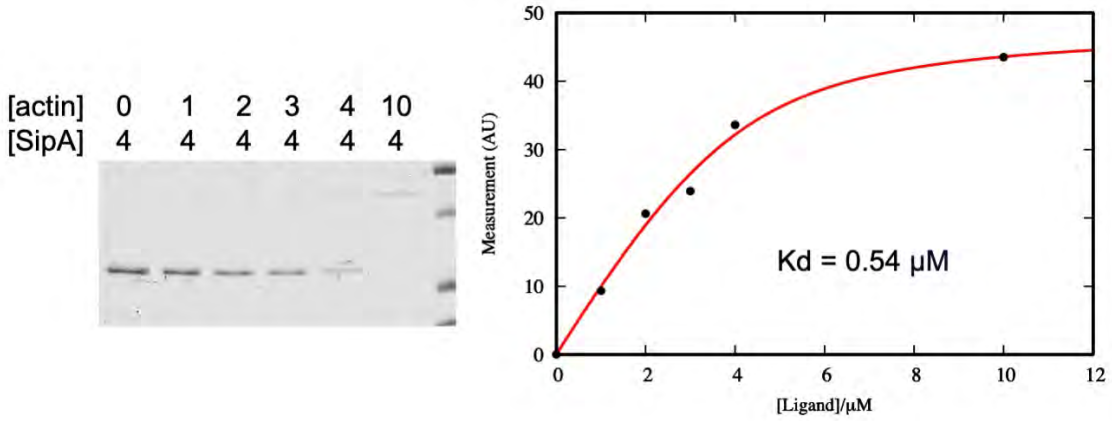

Supplementary Fig. 2. Actin-binding affinity of SipA$_{447-685}$. The binding affinity between purified SipA and actin filament as determined by a co-sedimentation assay.

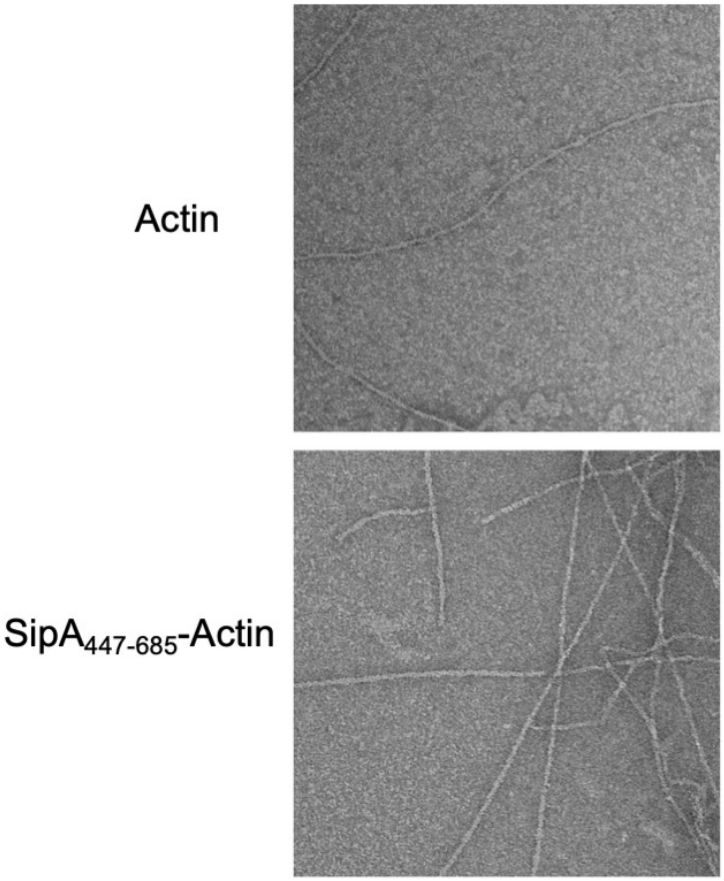

Supplementary Fig. 3. Representative negative staining electron microscopy images of actin and $SipA_{447-685}$ decorated actin

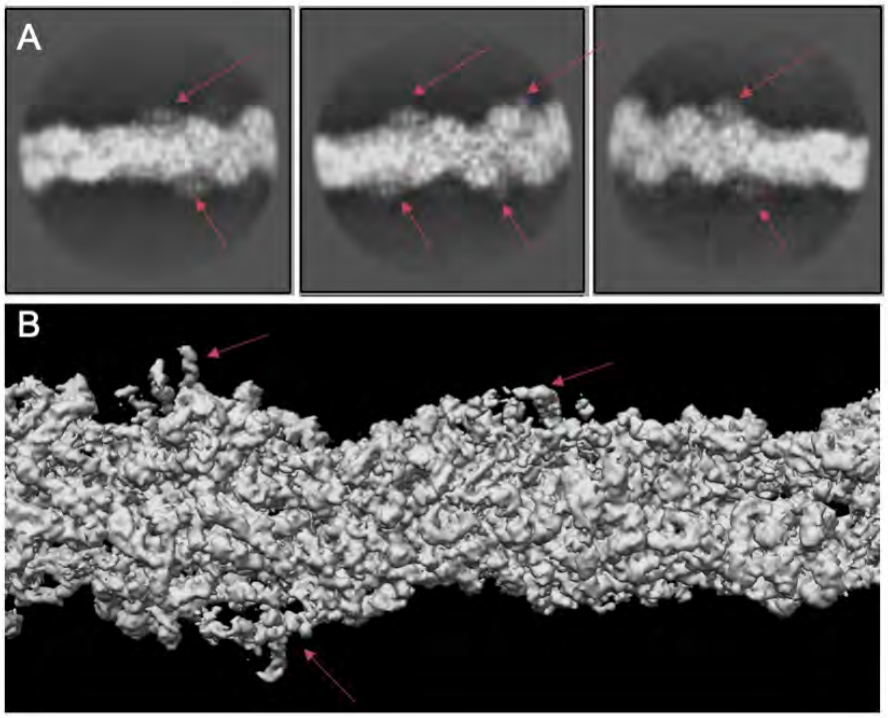

Supplementary Fig. 4. Lower electron map occupancy of SipA$_{446\text{-}684}$ in actin filaments. (**A**) representative 2D class averages of SipA$_{447\text{-}685}$ decorated actin filaments. Arrows show the density of SipA$_{447\text{-}685}$. (**B**) Initial 3D reconstruction of SipA$_{447\text{-}685}$ decorated actin filaments. Arrows show the density of SipA$_{447\text{-}685}$.

.

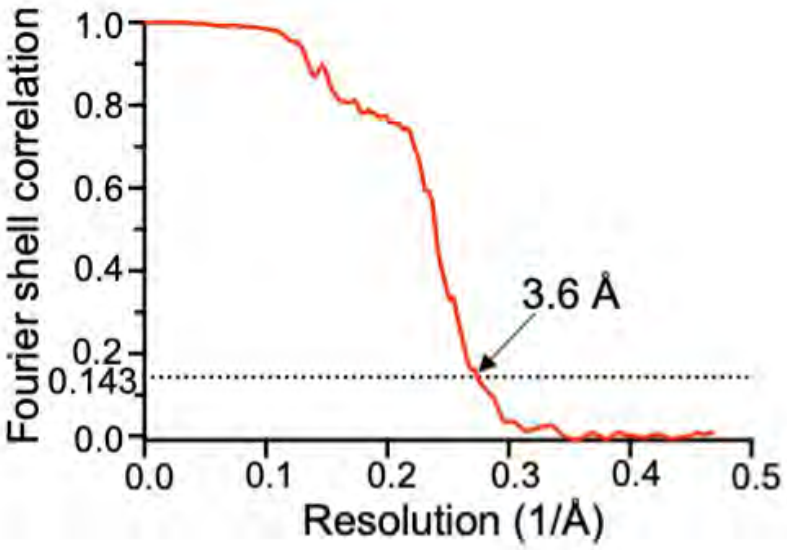

Supplementary Fig. 5. Global resolution estimation of the SipA$_{446\text{-}684}$-actin complex. Fourier shell correlation for maps constructed from two half data sets. A cutoff value of 0.143 is used.

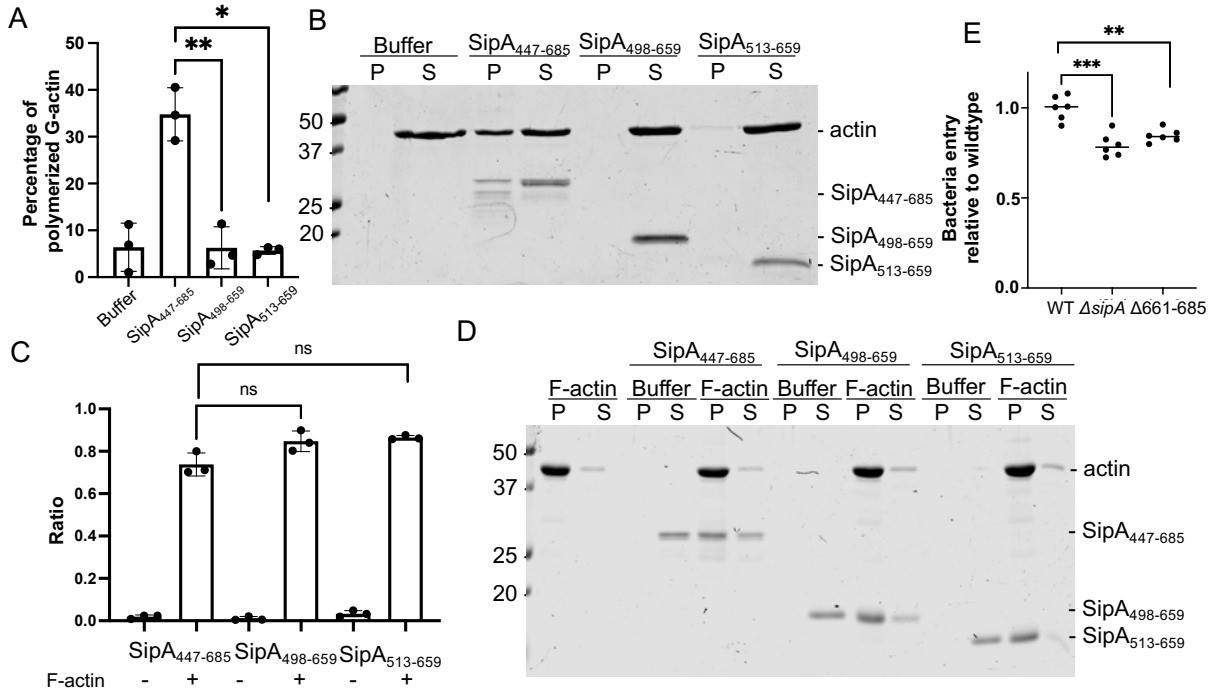

Supplementary Fig. 6. The unstructured arm regions are not necessary for the G-actin nucleation function of SipA but are dispensable for its ability to stabilize F-actin. (**A** and **B**) G-actin nucleation activity of different SipA constructs as determined by a co-sedimentation assay. Values shown in (**A**) are the mean ± SD of three independent experiments (*: P<0.05; **: P<0.01; unpaired two-sided t-test). (**C** and **D**) F-actin binding activity of different SipA constructs as determined by a co-sedimentation assay. Values shown in (**C**) are the mean ± SD of three independent experiments (ns: differences not significant, unpaired two-sided t-test). (**E**) A SipA mutant lacking the unstructured C-terminal region exhibits reduced invasion ability. The invasive ability of the different strains was measured by the gentamicin protection assay as described in the methods. Values represent the percentage of the inoculum that survived antibiotic treatment due to internalization and are the mean ± SD of six independent determinations normalized to wild type, which was set to 1. (**: P<0.01; ***: P<0.001; unpaired two-sided t-test). WT: wild type.

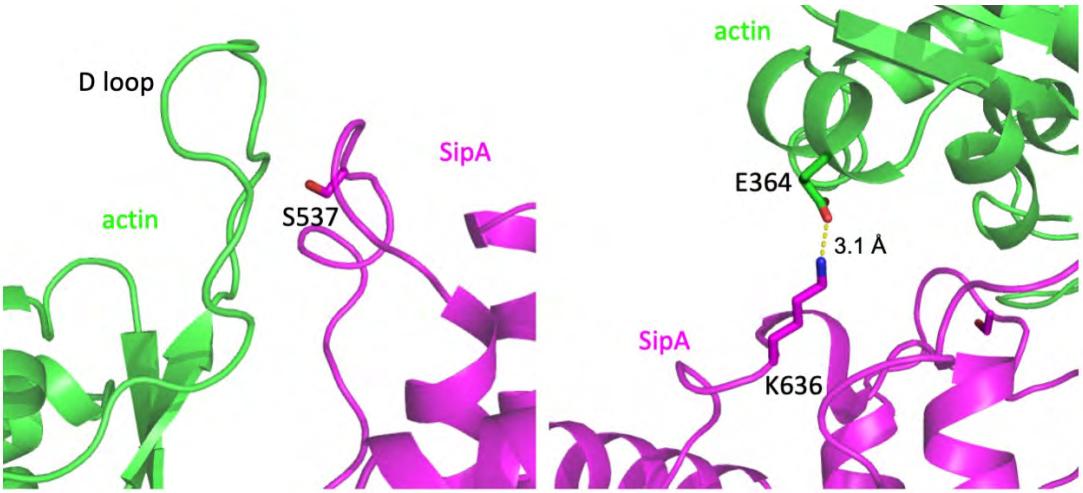

Supplementary Fig. 7. Residues S537 and K636 of SipA interact with the D-loop and C-terminus of actin. Interfaces between SipA (magenta) and actin (green) are shown. Interface residues S537 and K635 of SipA, as well as the D loop and the C-terminal residue E364 of actin are indicated.

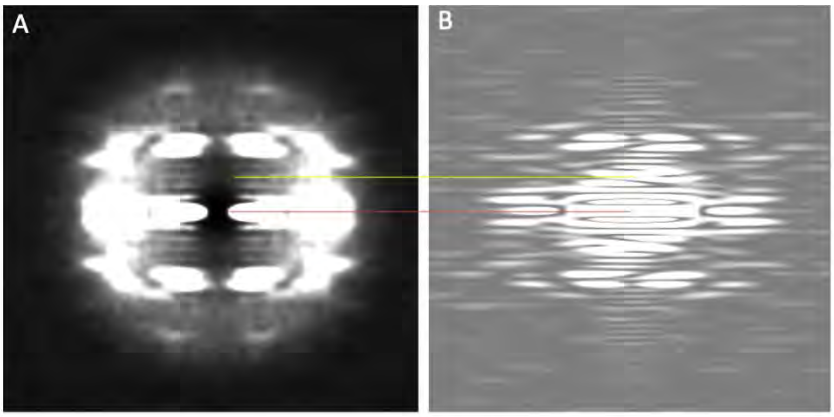

Supplementary Fig. 8. Power spectra of actin filaments decorated with SipA. (**A**) Averaged power spectrum of helix segments boxed out from 1300 micrographs. (**B**) Averaged power spectrum of map projections. Equator line (n = 0; l = 0) and rise line (n = 0; l = 17) are indicated with red and yellow lines, respectively. Rise = (pixel size) × (layer-line image size)/(layer-line height) = 1.068 × 4,096/39.91 = 109.6Å.